

# A Soft, Steerable Continuum Robot That Grows via Tip Extension

Joseph D. Greer,<sup>1</sup> Tania K. Morimoto,<sup>2</sup> Allison M. Okamura,<sup>1</sup> and Elliot W. Hawkes<sup>3</sup>

## Abstract

Soft continuum robots exhibit access and manipulation capabilities in constrained and cluttered environments not achievable by traditional robots. However, navigation of these robots can be difficult due to the kinematics of these devices. Here we describe the design, modeling, and control of a soft continuum robot with a tip extension degree of freedom. This design enables extremely simple navigation of the robot through decoupled steering and forward movement. To navigate to a destination, the robot is steered to point at the destination and the extension degree of freedom is used to reach it. Movement of the tip is always in the direction tangent to the end of the robot's backbone, independent of the shape of the rest of the backbone. Steering occurs by inflating multiple series pneumatic artificial muscles arranged radially around the backbone and extending along the robot's whole length, while extension is implemented using pneumatically driven tip eversion. We present models and experimentally verify the growing robot kinematics. Control of the growing robot is demonstrated using an eye-in-hand visual servo control law that enables growth and steering of the robot to designated locations.

**Keywords:** growing robot, robotic growth, continuum robot, soft robot control, biomimetic robots

## Introduction

**B**ECAUSE OF THEIR slender, continuously deformable, and compliant structures, continuum robots are useful for applications that require manipulation in or navigation through space-constrained and unstructured environments. Application areas of continuum robots are diverse and include minimally invasive surgery,<sup>1–3</sup> search and rescue,<sup>4</sup> and inspection.<sup>5,6</sup> However, their continuum nature introduces a new set of challenges for modeling and control compared with their rigid counterparts.<sup>7,8</sup> In particular, environmental contacts and disturbances may drastically alter the kinematics and dynamics of the robot bodies.<sup>9</sup> In this article, we introduce a new soft pneumatic continuum robot with a tip extension degree of freedom that permits movement of the robot's tip in a direction that is always tangent to the end of the robot's backbone, independent of environmental contacts and disturbances that may alter the shape of the rest of the backbone (Fig. 1). Among other benefits, this design simplifies control of the robot because steering and forward motion are decoupled.

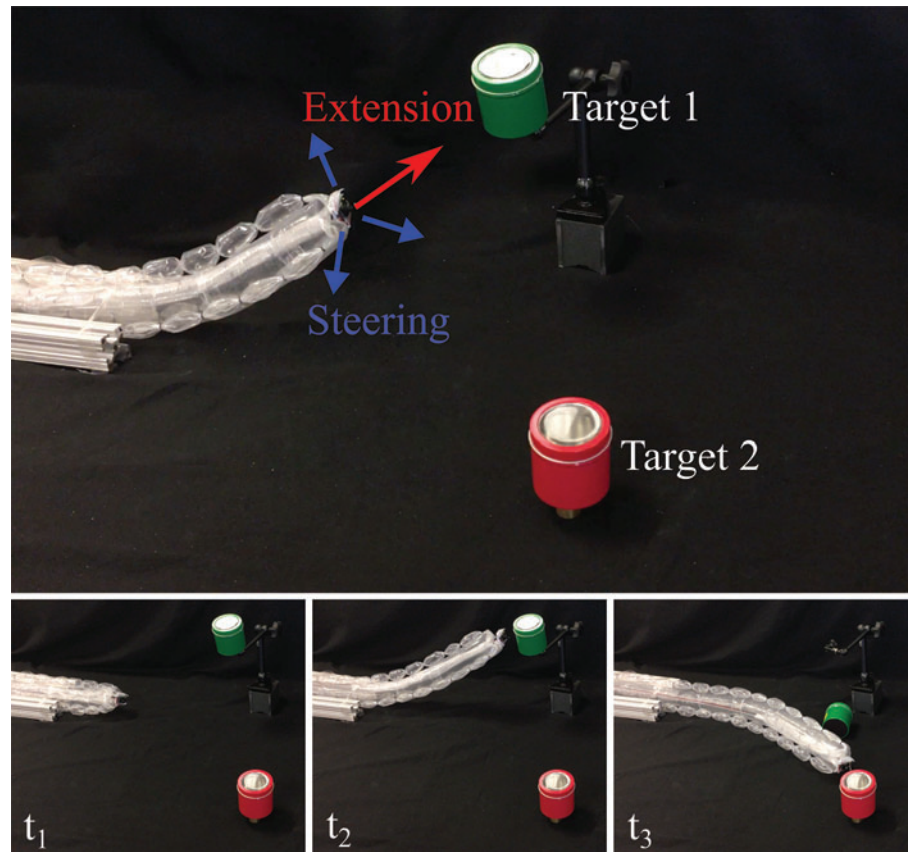
One method previously explored in the literature for changing the length of a continuum robot is through co-tensioning the robot's tendons. By using a pneumatic backbone and simultaneously controlling tendon tensions and backbone pressure, extension of the robot's backbone can be controlled. This extension is uniform along the backbone, instead of concentrated at the tip, and does not allow for fully decoupled steering and forward movement. Examples of robots that use this method include the Air-Octor robot of McMahan *et al.*<sup>10</sup> and the tentacle manipulator of Immega and Antonelli.<sup>11</sup> In this work, extension is achieved using pneumatically driven tip eversion. This method of growth was described by Mishima *et al.*<sup>12</sup> in 2003, without steering. Rösch *et al.*<sup>13</sup> and Sadeghi *et al.*<sup>14</sup> also developed devices that moved using tip eversion, where tip eversion is driven by a motor rather than air pressure. Those devices were developed to penetrate granular material.<sup>15,16</sup> Using a variant of tip eversion, Tsukagoshi *et al.*<sup>17</sup> developed an extending robot that was steerable by manual control. More recently, Hawkes *et al.* applied the concept of tip eversion to create a growing robot<sup>18</sup> made of thin-walled polyethylene tubing. This method demonstrated a robot that

<sup>1</sup>Department of Mechanical Engineering, Stanford University, Stanford, California.

<sup>2</sup>Department of Mechanical and Aerospace Engineering, University of California San Diego, La Jolla, California.

<sup>3</sup>Department of Mechanical Engineering, University of California Santa Barbara, Santa Barbara, California.

**FIG. 1.** Demonstration of soft continuum robot with an extension degree of freedom. Extension is implemented with pneumatically driven tip eversion<sup>18</sup> and simplifies motion control of the robot's tip by decoupling steering and movement. The bottom row shows a sequence in which the robot autonomously navigates to Target 1, pushes the target off its perch, and then steers and lengthens to reach Target 2. Times in the sequence  $t_1$ ,  $t_2$ , and  $t_3$  are spaced  $\sim 2$  s apart. This demonstration is provided in the Supplementary Video S1 (Supplementary Data are available online at [www.liebertpub.com/soro](http://www.liebertpub.com/soro)). Color images available online at [www.liebertpub.com/soro](http://www.liebertpub.com/soro)



could grow in length by two orders of magnitude. It was steered using discrete heading changes along its backbone that were permanent; once a turn was made, it could not be undone. The soft robot we present in this article uses the same method of growth, but a different method of turning—reversible bending of the soft growing robot body.

Bending in our soft robot is achieved using series pneumatic artificial muscles (sPAMs)<sup>19</sup> that are attached along the length of the robot's body (Fig. 2). The sPAMs cause reversible bending by exerting a tension force on the robot body and play a similar role to actuated tendons in traditional continuum robots.<sup>20</sup> An sPAM is a type of pneumatic artificial muscle (PAM),<sup>21</sup> which is a class of contractile actuators that turn the potential energy of compressed gas into mechanical work. Other examples of PAMs include McKibben muscles,<sup>22</sup> pouch motors,<sup>23</sup> pleated PAMs (PPAMs),<sup>24</sup> inverse PAMs,<sup>25</sup> and antagonistic PAMs.<sup>26</sup> As required by the extension degree of freedom of our soft robot, sPAMs are entirely soft. This allows them to withstand the large deformations that are experienced by the robot body and actuators as they unfurl from the tip during the eversion process (Fig. 2).

To steer the robot, we present an eye-in-hand visual servo-based heading controller.<sup>27</sup> A camera at the robot's tip (Fig. 2), whose optical axis is aligned with the robot's tip heading, provides a point-of-view image from the robot's perspective. Using this image, an operator may designate a destination (e.g., an object of interest). Growth of the robot will result in the robot moving toward the destination. The reversibility of the bending actuators provides three advantages over the irreversible turning system presented in Hawkes *et al.*<sup>18</sup> First, the robot can reach multiple targets in

one growth cycle. Second, mistakes in steering can be corrected. Third, the operator can reorient the robot/camera to look at different features in its environment without having to grow to reorient.

This article is organized as follows. The Hardware section describes the design and fabrication of the growing robot. The Physical Robot Modeling section develops a model for the kinematics of steering of the robot, which relates sPAM pressures and robot length, controlled by growth, to the location of the robot tip. The Steering Control section introduces and analyzes a visual servo-based steering controller and demonstrates its effectiveness in tasks requiring the robot to steer to a goal location. A preliminary version of portions of this work appeared in conference form in Greer *et al.*,<sup>19</sup> which introduced the sPAM actuator and steering of a *fixed length* robot. This study significantly extends<sup>19</sup> by adding growth as a degree of freedom to the robot, resulting in new models, control approaches, and robot capabilities.

## Hardware

### Robot

The construction of the robot is largely the same as the robot described in Greer *et al.*,<sup>19</sup> with several key modifications to enable length extension. It is composed of a backbone and three sPAMs attached via double-sided tape radially around the backbone (Fig. 1). Both the backbone and the sPAMs start as flat sheets of thin-walled polyethylene tubing of length  $L$  (Fig. 3a). When inflated, the thin-walled polyethylene tubing takes on the shape of a cylinder with diameter  $\frac{2W}{\pi}$  (Fig. 3b). To create an sPAM, rubber o-rings are placed

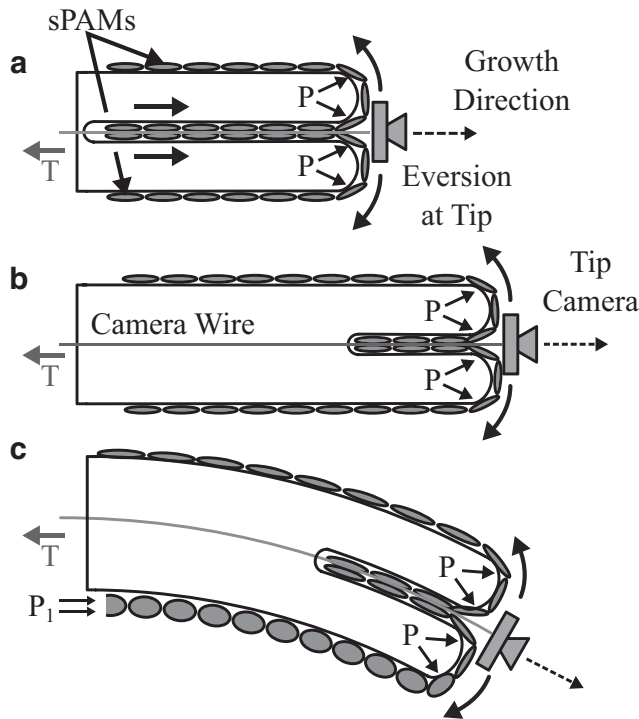


**FIG. 2.** Diagram of tip eversion-based growth and steering, with a camera payload. (a) Growing robot in initial configuration. The body internal pressure,  $P$ , causes robot body and sPAMs, which are attached to the body along its length, to evert at the tip of the robot. Growth direction is indicated by the dashed arrow and is always approximately aligned with tip camera's optical axis. (b) After a period of time, the robot has lengthened as a result of the growth process. The tension force,  $T$ , on the camera wire keeps the camera positioned at the distal end of the robot. (c) Pressurizing the lower sPAM to a pressure,  $P_1$ , causes it to bulge and contract, resulting in constant curvature bending of the robot body downward. sPAMs, series pneumatic artificial muscles.

onto a tube at regular intervals along the length of the tube, creating a series of actuator segments among which air can flow. When the sPAM is inflated, the profile of each actuator segment between o-rings becomes bulged when compared with its deflated state (Fig. 3c). Because polyethylene does not stretch significantly, the length of the actuator contracts when inflated due to its bulged profile (Fig. 3d). The length of maximum contraction is denoted by  $l_{eq}$  and is achieved when no tension force is applied to the actuator, as shown in Figure 3d.

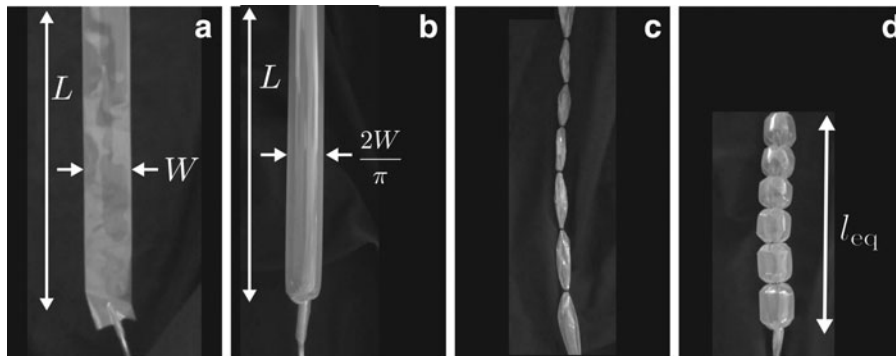


**FIG. 3.** Construction of an sPAM. sPAM consists of a length of thin-walled polyethylene tubing shown deflated in (a) and inflated in (b). Placing o-rings at regular intervals along its length (c) causes it to bulge and contract when inflated (d).

The robot's backbone can be thought of as a cantilevered beam whose stiffness is derived from its internal pressure. Similar to the motor-actuated tendons in certain continuum manipulators,<sup>20</sup> the sPAMs exert bending moments on the pneumatic backbone to cause reversible bending of the robot. The three sPAMs provide controllability of the robot's yaw and pitch.

To place the robot in a state ready for growth, the assembled backbone and sPAMs are inverted and pushed into the center of the backbone until the backbone length is a fraction of its original length. When the main tube is pressurized, the robot everts from the tip and grows back to its original length as shown in Figure 2. During the growth process, a camera is kept at the tip of the robot by applying a constant tension force on the camera wire. This force can be supplied by hand or through other means such as a weight, friction clamp, or actuator. The backward tension on the camera also serves to throttle the rate of growth of the robot.

Several hardware modifications were made to the robot design presented in Greer *et al.*<sup>19</sup> to enable growth of the robot. First, the camera could no longer be rigidly attached to the robot's tip, since this would prevent the tip eversion process. As a result, the camera was free to roll about its optical axis. To measure and compensate for camera roll, we attached an inertial measurement unit (IMU) to the camera. (See the Camera Rotation section for more details.) Second, the sPAMs were taped directly to the robot's body rather than using heat bonded polyethylene guides since the guides added resistance to the growth process. Finally, both the back of the camera and electronic wires fed through the middle of the robot were wrapped in Teflon to reduce friction between the robot's body and camera.

### Pneumatic system

To control the growth rate and heading of the growing robot, pressure in the main tube and each of the three sPAMs is regulated. The main tube is controlled to a pressure appropriate for growth, between 6.9 and 20.7 kPa. Pressure in each sPAM is dynamically adjusted during the course of growth of the robot to achieve a desired heading. A successive loop closure-based control architecture is used to steer the robot. Pressure set points for the pneumatic backbone and three sPAMs are regulated at 500 Hz by an inner pressure control loop. An outer visual servo control loop determines pressure set points at 30 Hz (Vision System section). The inner pressure control loop regulates pressures in each of the sPAMs by means of three electronic proportional valves (EV-

P-20-6050; Clippard Incorporated, Cincinnati, OH), controlling air flow rates and analog pressure sensors (MPX5100DP-ND; Freescale Semiconductor, Austin, TX) that are used for feedback.

### Vision system

As explained in the Steering Control section, an eye-in-hand visual servo control law<sup>27</sup> is used to control the orientation of the robot's tip to align with a user-defined goal position. Visual features are observed using a 170° field-of-view miniature camera (AccFly, Shenzhen, China) mounted at the tip of the continuum robot (Fig. 2). Image processing is performed by dedicated hardware (SightLine Applications Incorporated, Hood River, OR) at 30 Hz. Information from the image processing hardware is communicated to the control system via RS-232.

### Physical Robot Modeling

In this section, we develop relationships between the pressure inside each of the three sPAMs attached to the robot's body and the body's position in space. We start by summarizing results from Greer *et al.*<sup>19</sup> that govern the kinematic relationship between a change in pressure in each of the three sPAMs and displacement of the tip. We then incorporate the extension degree of freedom into the robot's kinematic model and show that when the robot is extended with constant turning actuator pressure, its tip will extend along a constant curvature arc. This has implications for the visual servo control described in the Visual Servo Control Law section. We conclude with an analysis of the workspace of the robot.

#### Steering kinematics

In this section, we summarize the relationship between pressures in the three sPAMs and the position and orientation of the robot's tip. The relationship is in the form of a system of equations that are derived in Greer *et al.*,<sup>19</sup> using static equilibrium analysis. We present the equations and describe the relevant variables, as they are used later in the article.

**sPAM model.** When the o-ring spacing of sPAMs is below a threshold, the behavior of the actuators is identical to the behavior of PPAMs. PPAMs were characterized by Daerden and Lefebvre<sup>28</sup> and have a known force/displacement relationship. The force/displacement curve of sPAMs was shown in Greer *et al.*<sup>19</sup> to have two important properties for the purposes of kinematic modeling:

1. For a fixed pressure, the force/displacement curve is approximately linear (Fig. 4a).

2. For a given displacement, force scales linearly with pressure, which may be seen from the length to load relationship of PAMs<sup>24</sup>:

$$F = -p \frac{dV}{dL} \quad (1)$$

where  $F$  is the force exerted by the actuator,  $p$  is the pressure inside the actuator,  $V$  is the volume inside the actuator, and  $L$  is the length of the actuator along the direction  $F$  acts.

Given these two properties, we approximate each of the three sPAMs as linear springs with constant equilibrium lengths (Figs. 3d and 4b). Increasing or decreasing the pressure inside an sPAM changes the spring stiffness of the sPAM accordingly:

$$F_i = K_i(l_i - l_i^{eq}) \quad \text{for sPAM } i = 1, 2, 3 \quad (2)$$

where

$$K_i = p_i k_i \quad \text{for sPAM } i = 1, 2, 3 \quad (3)$$

and  $F_i$  is the tension force,  $K_i$  is the spring stiffness,  $l_i$  is the length,  $l_i^{eq}$  is the equilibrium length,  $p_i$  is the pressure, and  $k_i$  is the scaling constant relating pressure to spring stiffness of the  $i^{th}$  sPAM.

**Kinematic relationship.** As explained in the Hardware section, three sPAMs are attached radially around the robot's backbone and enable control of the orientation of the tip of the robot in yaw and pitch. In this section, we describe a system of equations that relates the position and orientation of the tip of the robot,  $\vec{x}_{ef}$ ,  $R_{ef}$ , to the three sPAM pressures,  $p_1$ ,  $p_2$ , and  $p_3$ . The equations presented below are derived using the simplifying assumption that the tension force exerted by the sPAMs causes the robot to bend in a constant curvature arc,<sup>8</sup> using static equilibrium analysis in Greer *et al.*<sup>19</sup> The bending and axial stiffnesses of the robot's backbone are represented as torsional and linear springs, respectively. Table 1 summarizes the notation used in the kinematic model.

The first three (of six) equations of the kinematic model relate the lengths of the actuators to the robot's arc-space parameters:

$$l_i = l - \theta(D_{tube}/2) \cos \phi_i \quad \text{for sPAM } i = 1, 2, 3 \quad (4)$$

The other three equations come from static equilibrium analysis. They are expressed as two vector equations below

**FIG. 4.** Force/displacement curves predicted by sPAM model presented in Greer *et al.*<sup>19</sup> Each curve corresponds to an actuator pressure (a) and is well approximated as linear springs whose stiffness is modulated linearly by controlling pressure inside the actuator (b).

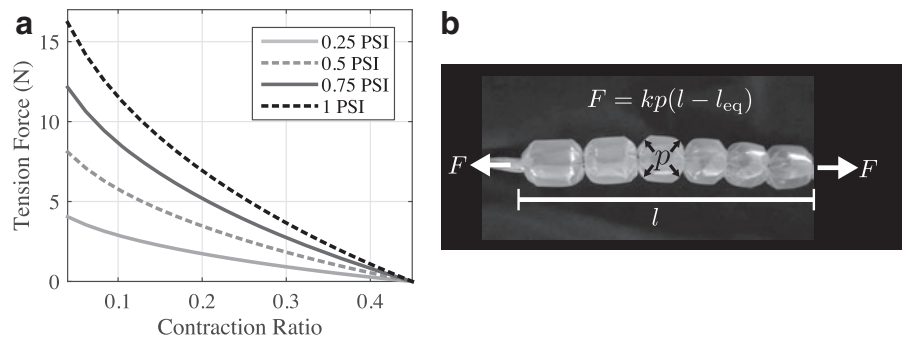




TABLE 1. NOTATION

$\hat{x}, \hat{y}, \hat{z}$	Global coordinate axes
$\hat{x}_{\text{ef}}, \hat{y}_{\text{ef}}, \hat{z}_{\text{ef}}$	Tip coordinate axes. $R_{\text{ef}} = [\hat{x}_{\text{ef}}, \hat{y}_{\text{ef}}, \hat{z}_{\text{ef}}]$
$l, \phi, \theta$	Arc-space parameters <sup>8</sup> (Fig. 5a–c)
$l_1, l_2, l_3$	Actuator lengths
$\psi_1, \psi_2, \psi_3$	Actuator positions, specified in radians (Fig. 5b)
$\phi_1, \phi_2, \phi_3$	$\phi_i = \psi_i - \phi$
$k_1, k_2, k_3$	Pressure-spring constants of sPAMs (Eq. 2)
$K, K_t$	Backbone axial and torsional stiffness

sPAMs, series pneumatic artificial muscles.

(force and moment balance, respectively), and reduce to three scalar equations:

$$\left( \sum_{i=1}^3 -k_i p_i (l_i - l_i^{\text{eq}}) - K(l - l^{\text{eq}}) \right) \hat{z} = 0 \quad (5)$$

$$\sum_{i=1}^3 \left( \frac{D_{\text{tube}}}{2} k_i p_i (l_i - l_i^{\text{eq}}) R_z(\psi_i) \right) \hat{y} - K_t \theta R_z(\phi) \hat{y} = 0 \quad (6)$$

where  $R_z(\cdot)$  is a rotation about  $[0, 0, 1]^T$  by a specified number of radians.

Finally, with  $l, \phi$ , and  $r$  computed, the end-effector position can be computed. We define a coordinate system whose origin is at the base of the robot's backbone curve and coordinate axes that are parallel to those shown in Figure 5a. With this coordinate system definition, we write  $\vec{x}_{\text{ef}}$  and  $R_{\text{ef}}$  as

$$\vec{x}_{\text{ef}} = r(\cos(\theta) - 1)\hat{w} + r\sin(\theta)\hat{z} \quad (7)$$

$$\hat{w} = [\cos(\phi) \sin(\phi) 0]^T \quad (8)$$

$$R_{\text{ef}} = R_v(\theta) \quad (9)$$

$$\hat{v} = [\sin(\phi) \cos(\phi) 0]^T \quad (10)$$

### Kinematics of growth and steering

Because backbone equilibrium length continuously increases during the growth process, we further analyze the effect backbone equilibrium length has on the kinematics of steering. As explained in the Kinematic Relationship section, Equations 4, 5, and 6 provide six scalar equations in six unknowns that can be solved for: bending plane angle, radius of curvature, backbone length, and three side lengths ( $\phi, r, l, l_1, l_2, l_3$ ). These equations are a function of known sPAM pressures,  $p_1, p_2, p_3$ , and robot geometry, including backbone equilibrium length,  $l^{\text{eq}}$ . To analyze the effect of growth on steering kinematics, we assume that  $p_1, p_2, p_3$  remain constant, and consider what happens if the backbone equilibrium length is changed from  $l^{\text{eq}}$  to  $\alpha l^{\text{eq}}$ , for some constant  $\alpha > 0$ . The main result is that if the robot is grown with constant sPAM pressures, bending plane angle and curvature will remain constant.

To show this, we first return to the geometric relationship of Equation 4 and assume that  $l_i, \theta, \phi$  satisfy this equation for the original length,  $l$ :

$$l_i = l - \theta(D_{\text{tube}}/2) \cos \phi_i \quad \text{for sPAM } i = 1, 2, 3 \quad (11)$$

Assuming this is true, then arc-space parameters  $\alpha l_i, \alpha \theta, \phi$  will satisfy the equation for new backbone length,  $\alpha l$ :

$$\alpha l_i = \alpha l - \alpha \theta(D_{\text{tube}}/2) \cos \phi_i \quad \text{for sPAM } i = 1, 2, 3 \quad (12)$$

Now, we consider the static equilibrium conditions. Under standard linear and torsional spring scaling laws,<sup>29</sup> the main tube springs will have stiffness factors of  $1/\alpha$  compared with the original length,  $l$ :

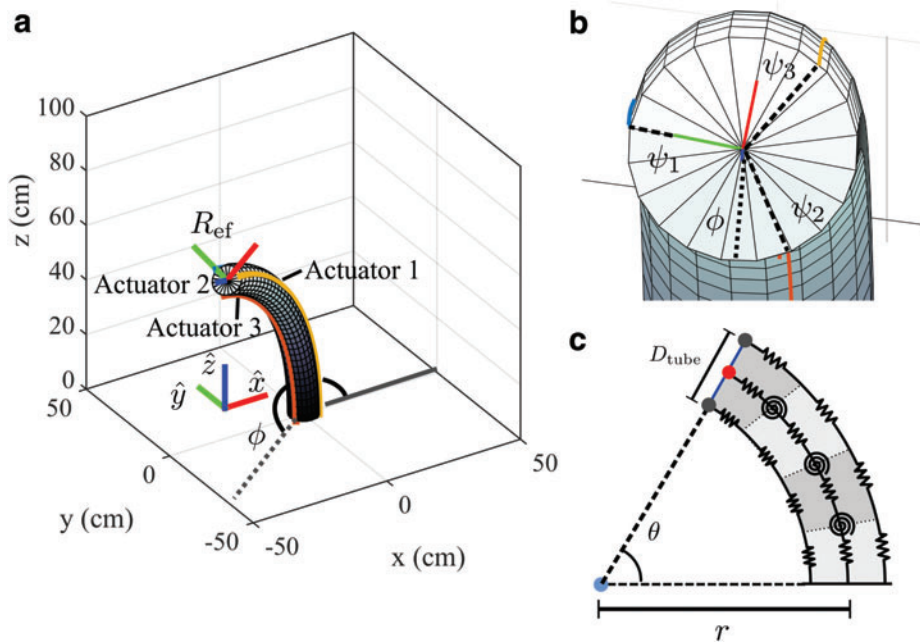


**FIG. 5.** Constant curvature robot parameters. (a) Three-dimensional rendering of constant curvature robot, actuator locations, tip frame, arc-space parameters, and coordinate system. (b) Head on view of robot tip with relevant variables labeled. (c) Arrangement of discrete spring system used for kinematic model. Color images available online at [www.liebertpub.com/soro](http://www.liebertpub.com/soro)

$$K^{(\alpha)} = K/\alpha \quad (13)$$

$$\kappa^{(\alpha)} = \kappa/\alpha \quad (14)$$

$$K_i^{(\alpha)} = K_i/\alpha \quad (15)$$

where  $K^{(\alpha)}$ ,  $\kappa^{(\alpha)}$ ,  $K_i^{(\alpha)}$  denote the underlying stiffnesses of the robot with length  $\alpha l$ . Evaluating the static equilibrium equations (Eqs. 5 and 6) with the new arc-space parameters and stiffnesses, we get the following:

$$\left( \sum_{i=1}^3 -\frac{K_i}{\alpha}(\alpha l_i - \alpha l_i^{\text{eq}}) - \frac{K}{\alpha}(\alpha l - \alpha l^{\text{eq}}) \right) \hat{z} = 0 \quad (16)$$

and

$$\left( -\sum_{i=1}^3 \frac{D_{\text{tube}} K_i}{2} \frac{K_i}{\alpha}(\alpha l_i - \alpha l_i^{\text{eq}}) R_z(\psi_i) - \frac{\kappa}{\alpha} \alpha \theta R_z(\phi) \right) \hat{x} = 0 \quad (17)$$

The parameter  $a$  can be canceled from the above two equations. From this it follows that if arc-space parameters  $l_i, \theta, \phi$  satisfy the equilibrium conditions for a robot with equilibrium length  $l^{\text{eq}}$ , then  $\alpha l_i, \alpha \theta, \phi$  will satisfy the equilibrium conditions for a robot with backbone equilibrium length  $\alpha l^{\text{eq}}$ .

This establishes the expected relationship between arc-space parameters of two robots with the same actuator pressures,  $p_1, p_2, p_3$ , but different equilibrium lengths,  $l^{\text{eq}}$ , and  $\alpha l^{\text{eq}}$  (Fig. 6): the bending plane angle is conserved and the curvature of the robot will be the same ( $\theta/l = \alpha \theta/\alpha l$ ).

### Physical Jacobian

In this section, we explain how to compute the kinematic model's Jacobian,  $J \in \mathbb{R}^{6 \times 4}$ , which maps from joint-space velocities (i.e., growth rate,  $\dot{\alpha}$ , and pressure derivatives,  $\dot{p}_1, \dot{p}_2, \dot{p}_3$ ) to the end-effector twist (linear and angular velocities):

$$[\dot{\vec{x}}_{\text{ef}}, \dot{\vec{\omega}}]^\top = J[\dot{\alpha}, \dot{p}_1, \dot{p}_2, \dot{p}_3]^\top \quad (18)$$

We decompose  $J$  as the product of two matrices,  $J_1 \in \mathbb{R}^{6 \times 4}$ ,  $J_2 \in \mathbb{R}^{6 \times 6}$ :

$$J = J_2 J_1 \quad (19)$$

$J_1$  maps joint-space velocities to arc-space parameter time derivatives:

$$[\dot{\phi}, \dot{\theta}, \dot{l}_1, \dot{l}_2, \dot{l}_3]^\top = J_1[\dot{\alpha}, \dot{p}_1, \dot{p}_2, \dot{p}_3]^\top \quad (20)$$

and  $J_2$  maps arc-space parameter time derivatives to end-effector twist:

$$[\dot{\vec{x}}_{\text{ef}}, \dot{\vec{\omega}}]^\top = J_2[\dot{\phi}, \dot{\theta}, \dot{l}_1, \dot{l}_2, \dot{l}_3]^\top \quad (21)$$

Because we do not have a closed-form solution relating joint-space parameters to arc-space parameters (Kinematics

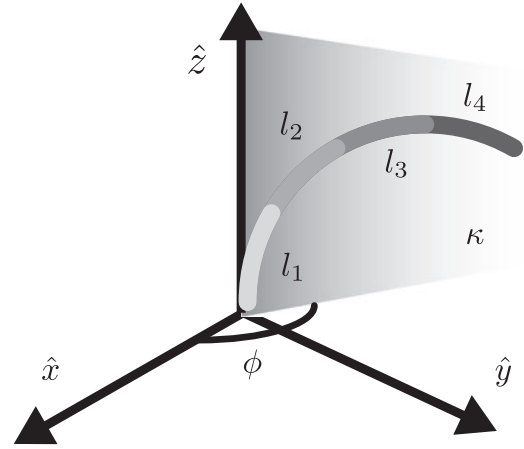


**FIG. 6.** Kinematics of the robot during growth. Equations 19 and 25 show that bending plane angle,  $\phi$ , and backbone curvature,  $\kappa$ , will be constant during growth if sPAM pressures are constant.

of Growth and Steering section), we use the implicit function theorem to compute  $J_1$ :

$$J_1 = - \overbrace{\begin{bmatrix} \frac{\partial f_1}{\partial \phi} & \dots & \frac{\partial f_1}{\partial l_3} \\ \vdots & \ddots & \vdots \\ \frac{\partial f_6}{\partial \phi} & \dots & \frac{\partial f_6}{\partial l_3} \end{bmatrix}}^{6 \times 6}^{-1} \overbrace{\begin{bmatrix} \frac{\partial f_1}{\partial \alpha} & \dots & \frac{\partial f_1}{\partial p_3} \\ \vdots & \ddots & \vdots \\ \frac{\partial f_6}{\partial \alpha} & \dots & \frac{\partial f_6}{\partial p_3} \end{bmatrix}}^{6 \times 4} \quad (22)$$

where  $f_1, \dots, f_6$  are the kinematic constraint equations relating joint-space parameters to arc-space parameters (Eqs. 12, 16, and 17).

The equations relating arc-space parameters to position and orientation of the robot tip are explicit and therefore we compute  $J_2$  by simply differentiating the expressions for  $\vec{x}_{\text{ef}}$  and  $R_{\text{ef}}$  in equations 7 and 9 with respect to the arc-space parameters.

### Workspace analysis

Using the kinematic model developed in the Kinematic Relationship section and the Kinematics of Growth and Steering section, we can determine the set of points reachable by the tip of the growing robot, that is, the growing robot's workspace. The inputs that are controllable include the equilibrium length of the backbone of the growing robot,  $\alpha l^{\text{eq}}$ , and the sPAM pressures,  $p_1, p_2, p_3$ . To compute its workspace, we calculate the forward kinematics for each feasible input tuple:

$$(\alpha, p_1, p_2, p_3) \in [\alpha_{\min}, \alpha_{\max}] \times [0, p_{\max}]^3 \quad (23)$$

using Equations 4, 5, and 6.  $\alpha_{\min}$  and  $\alpha_{\max}$  represent the minimum and maximum backbone length ratios of the growing robot and  $p_{\max}$  is the bursting pressure of the sPAMs.

Figure 7 shows the workspace analysis for a robot that is 2 m long when fully extended. At a fixed length of 2 m, the robot tip can be steered along a set of points that is roughly a two-dimensional surface (Fig. 7a, c). We note that the steering surface is not exactly two dimensional as the sPAMs may be used to reduce the length of the robot's backbone in addition to changing the orientation of the tip. Growth adds

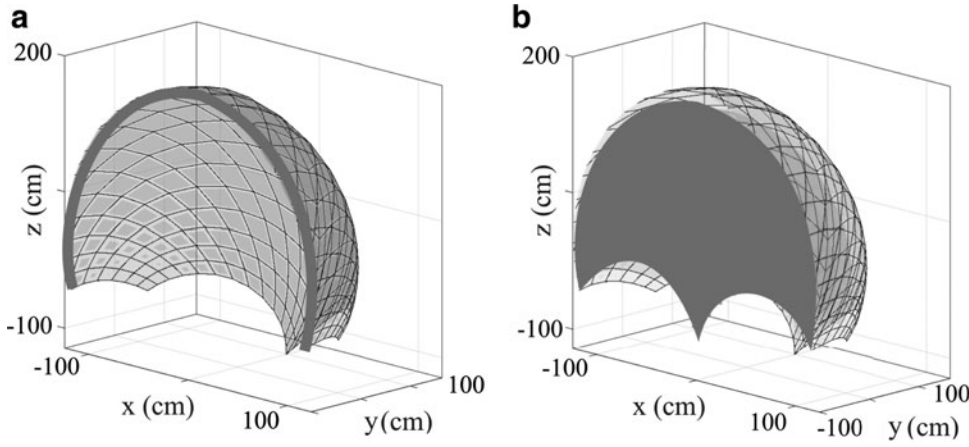


**FIG. 7.** Workspace analysis of the tip of a robot that can extend to 200 cm. Without growth, (i.e. steering only) the robot tip is effectively confined to a two-dimensional steering surface whose cross section at  $y=0$  is shown in (a). With growth, the robot's workspace encompasses a solid three dimensional volume that is the union of steering surfaces of robots whose lengths range 0 to 200 cm long. The workspace's cross section at  $y=0$  is shown in (b).

an independent degree of freedom that extends the workspace into a solid volume, which is the union of steering surfaces of robots whose backbone equilibrium lengths vary from 0 to 2 m (Fig. 7b, d).

### Steering Control

In this section, we present and analyze the controller used to steer the robot. As explained in the Introduction section, the robot's direction of growth is aligned with its tip tangent, and therefore, the robot will grow to an object of interest if its heading is aligned with the object. To achieve heading alignment, we use a camera at the robot's tip, whose optical axis is parallel to the tip's tangent (Vision System section), and an eye-in-hand visual servo controller (Fig. 8). The controller drives the object of interest's location within the camera's field of view to the center so that the robot's heading is aligned with the object.

#### Image space modeling

In this section, we derive the transformation from control inputs to image coordinates (Fig. 9), which is used in the visual servo control law. More concretely, using the notation of Chaumette,<sup>30</sup> we let  $\vec{s} \in \mathbb{R}^2$  be the image features we are interested in controlling (in this case, the image coordinates of the designated object we are tracking), and we let  $\vec{s}^* \in \mathbb{R}^2$ , be the desired coordinates of  $\vec{s}$  (in this case, the center of the image,  $[0, 0]^T$ ). We are interested in computing an image feature Jacobian,  $J_s \in \mathbb{R}^{2 \times 4}$ , that maps joint-space velocities,  $\vec{q} = [\dot{\alpha}, \dot{p}_1, \dot{p}_2, \dot{p}_3]^T$ , to image feature velocities,  $\dot{\vec{s}}$ :

$$\dot{\vec{s}} = J_s \vec{q} \quad (24)$$

$J_s$  is logically formed as the product of four matrices (Fig. 9):

$$J_s = L^c V_f^f V_n J \quad (25)$$

each described below, from right to left.

**Physical robot Jacobian.**  $J \in \mathbb{R}^{6 \times 4}$  is the physical robot Jacobian and maps from joint-space velocities to the end-

effector twist (linear and angular velocities). Its computation is described in the Physical Jacobian section.

**End-effector twist transformation.**  ${}^f V_n \in \mathbb{R}^{6 \times 6}$  is a transformation to map the end-effector twist  $\in \mathbb{R}^6$ , which is expressed in the global reference frame in which the kinematics is defined (Fig. 6) to the reference frame of the tip of the growing robot. In our case it is given by the following:

$${}^f V_n = \begin{bmatrix} R_{ef}^T & \mathbf{0}^{3 \times 3} \\ \mathbf{0}^{3 \times 3} & R_{ef}^T \end{bmatrix} \quad (26)$$

where  $R_{ef}$  is the orientation of the end-effector Equation 9.

**Camera twist transformation.**  ${}^c V_f \in \mathbb{R}^{6 \times 6}$  is a twist transformation mapping from the robot tip to the camera frame. Because the camera is free to rotate about the robot's backbone axis (Fig. 10), the two frames are related by a rotation of an unknown angle,  $\beta$ , that must be estimated (Camera Rotation section):

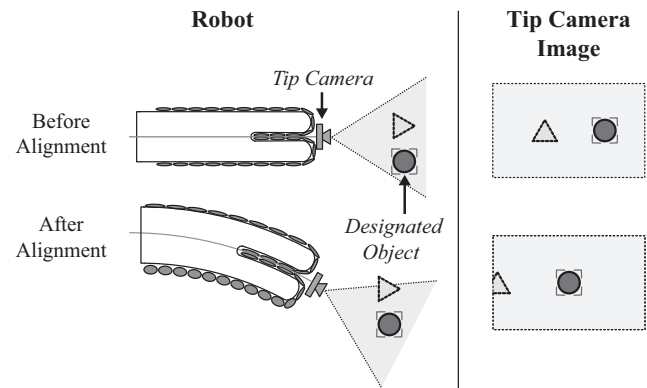


**FIG. 8.** Eye-in-hand visual servo control is a class of controllers that attempt to drive a designated image feature to a specified location in the camera's field of view (in our case the center). For the growing robot with a camera at its tip, this corresponds to aligning its heading with the designated feature, depicted in this figure as a circle.

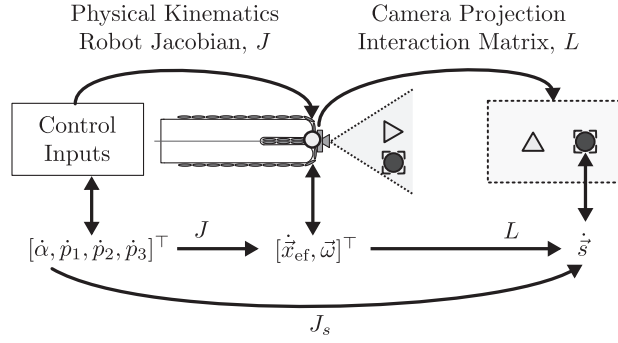


**FIG. 9.** Visual servo modeling components. Kinematic modeling from robot control inputs to image space consists of physical robot kinematics (Physical Jacobian section) and camera projection (Image Space Modeling section). The circle represents the designated feature in the robot's field of view to steer toward.

$${}^cV_f = \begin{bmatrix} R_z(\beta)^\top & \mathbf{0}^{3 \times 3} \\ \mathbf{0}^{3 \times 3} & R_z(\beta)^\top \end{bmatrix} \quad (27)$$

**Interaction matrix.**  $L$  is the interaction matrix that captures considerations of the camera formation process. In particular, it maps camera twist (expressed in the reference frame of the camera) to image feature velocities  $\dot{s}$ <sup>30</sup>:

$$\dot{s} = L \begin{bmatrix} \dot{x}_{ef} \\ \dot{\omega} \end{bmatrix} \quad (28)$$

In our case, the image feature we wish to control is the image coordinate of the designated object that the robot is being steered toward,  $\vec{s} = [s_x, s_y]^\top$ . Espiau *et al.* have derived the interaction matrix for this case in Espiau *et al.*<sup>31</sup> and it is given by

$$L = f \begin{bmatrix} -1/Z & 0 & x/Z & xy & -(1+x^2) & y \\ 0 & -1/Z & y/Z & 1+y^2 & -xy & -x \end{bmatrix} \quad (29)$$

where  $Z$  is the depth of the object relative to the camera and  $x, y$  are the normalized image coordinates of the goal object. They are related to pixel coordinates,  $[u, v]^\top$ , by the following relationship:

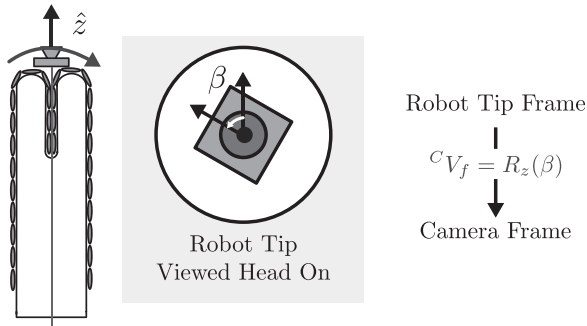


**FIG. 10.** Camera spin diagram. Camera is free to spin about the robot's backbone axis,  $\hat{z}$ , resulting in a rotation by an unknown amount  $\beta$  that must be estimated to compute the image Jacobian.

$$x = u/f \text{ and } y = v/f$$

assuming the principal point of the camera is at the origin of the image, and  $f$  is the focal length of the camera in pixels.

In this work, we are interested only in the last three columns of the image space Jacobian because we control the heading of the robot by modulating the pressure in each of the three sPAM actuators ( $p_1, p_2, p_3$ ) and not through growth ( $\alpha$ ). We refer to the reduced column Jacobian as  $J_r$  throughout the remainder of the article. Concretely we define  $J_r \in \mathbb{R}^{2 \times 3}$  as

$$J_r = J_s \begin{bmatrix} \mathbf{0}_{1 \times 3} \\ I_{3 \times 3} \end{bmatrix} \quad (30)$$

where  $\mathbf{0}_{1 \times 3}$  is a row of zeros and  $I_{3 \times 3} \in \mathbb{R}^{3 \times 3}$  is the identity matrix.

### Growing considerations

Consider the case that the growing robot is steering to a goal object far away ( $1/Z \approx 0$ ). In this section, we show that the reduced column image Jacobian,  $J_r$ , scales with length. This is an important consideration for controller stability as changes in joint-space parameters have magnified effects at longer lengths. The scaling of  $J_r$  with length is explained as follows.

In the case that  $1/Z \approx 0$ ,  $L$  reduces to

$$L \approx f \begin{bmatrix} 0 & 0 & 0 & xy & -(1+x^2) & y \\ 0 & 0 & 0 & 1+y^2 & -xy & -x \end{bmatrix} \quad (31)$$

This says that tip orientation and not tip position affects image feature coordinates (i.e., there is no parallax).

Let  $\theta, \phi, l$  be the arc-space parameters of a robot with equilibrium length  $l^q$  and let  $\theta_\alpha, \phi_\alpha, l_\alpha$  be the arc-space parameters of a robot with equilibrium length  $\alpha l^q$ . Then in the Kinematics of Growth and Steering section we have

$$\theta_\alpha = \alpha\theta, \quad \phi_\alpha = \phi, \quad l_\alpha = \alpha l \quad (32)$$

and therefore their velocities scale accordingly:

$$\dot{\theta}_\alpha = \alpha\dot{\theta}, \quad \dot{\phi}_\alpha = \dot{\phi}, \quad \dot{l}_\alpha = \dot{l} \quad (33)$$

It can be seen by inspection of Equation 9 that the magnitude of the angular velocity vector will scale linearly with  $\alpha$  since  $\dot{\theta}$  scales linearly with  $\alpha$ . Because  $L$  is nonzero only in the columns corresponding to angular velocity,  $J_r$  will scale linearly with  $\alpha$  as well.

### Visual servo control law

A standard visual servo control law as presented in Espiau *et al.*<sup>31</sup> and Chaumette and Hutchinson<sup>32</sup> can be used to drive the image feature error magnitude  $\vec{s}^* - \vec{s}$  to 0 (point the robot at the goal object):

$$\dot{\vec{q}} = \lambda J_r^+ (\vec{s}^* - \vec{s}) \quad (34)$$

where  $J_r^+$  is the pseudoinverse of  $J_r$ . This control law commands joint velocities that will lower the magnitude of the image feature error.



In this work, we modify the standard visual servo control law in two ways. First, we add damping to the image feature error that was empirically found to reduce controller-based oscillations and limit cycles:

$$\vec{e} = K_p(\vec{s}^* - \vec{s}) + K_d\dot{\vec{s}} \quad (35)$$

where  $K_p$  is the proportional term and  $K_d$  is the damping term.

Second, we use box-constrained least-squares optimization<sup>33</sup> to find joint velocities that will decrease the magnitude of the image error,  $\vec{e}$ , rather than the pseudoinverse of the image space Jacobian. We do this because the pseudoinverse of the image Jacobian does not respect joint-space limits (e.g., negative sPAM pressures are not physically realizable):

$$\dot{\vec{q}} = \arg \min_{0 \leq \dot{\vec{q}} \leq \dot{\vec{q}}_{\max}} \|J_r \dot{\vec{q}} - \vec{e}\|_2 \quad (36)$$

This was empirically found to reduce the rise time/settling time of the controller and improve stability compared with the standard pseudoinverse controller with clipping to actuator limit ranges.

#### Jacobian calibration

Our visual servo control law (Visual Servo Control Law section) relies on an accurate reduced column image space Jacobian,  $J_r$ . Due to the number of physical parameters used to calculate  $J_r$  that may vary between uses of the robot, we have elected to use an empirical image space Jacobian,  $\hat{J}_r$ , that is determined through a simple calibration process. This process is inspired by the work of Yip and Camarillo.<sup>9</sup>

We perform the calibration process at the beginning of each use, when the robot is in a straightforward configuration. Column  $i$  of  $J_r$  is determined by incrementing the corresponding joint-space variable,  $q_i$ , by some amount  $\delta q_i$  and monitoring its effect on the image feature vector,  $\vec{s}$ :

$$\hat{J}_r = [\vec{J}_r^{(1)} \quad \vec{J}_r^{(2)} \quad \vec{J}_r^{(3)}] \quad (37)$$

$$\vec{J}_r^{(i)} = \frac{\delta \vec{s}}{\delta q_i} \quad (38)$$

$$\delta \vec{s} = \vec{s} - \vec{s}_0 \quad (39)$$

where  $\vec{s}_0$  are the image coordinates of the designated object in its beginning location.

**Configuration considerations.**  $\hat{J}_r$  is used in place of  $J_r$  in the visual servo control law (Equation 30). We note that  $J_r$  is a function of its state and therefore varies throughout its workspace, yet  $\hat{J}_r$  is calibrated to  $J_r$  only in the straightforward configuration before growth. However, we have found that this Jacobian results in stable control. This is due to the consistency of the image Jacobian throughout the robot's workspace. Figure 11 shows an analysis of how well the image Jacobian in the straightforward configuration approximates the image Jacobian throughout its workspace. Both magnitude errors and direction errors were considered.

Normalized magnitude errors at each configuration were calculated as follows:

$$\text{mean}(|\vec{J}_s^{(i)}|_2 - |\vec{J}_{s0}^{(i)}|_2) / \text{mean}(|\vec{J}_s^{(i)}|_2) \quad \text{for } i = 1, 2, 3 \quad (40)$$

and direction errors were calculated as follows:

$$\text{mean}(\angle(\vec{J}_s^{(i)}, \vec{J}_{s0}^{(i)})) \quad \text{for } i = 1, 2, 3 \quad (41)$$

where  $J_r$  is the image Jacobian at a particular configuration,  $J_{s0}$  is the image Jacobian in the straightforward configuration, and  $\vec{J}_s^{(i)}, \vec{J}_{s0}^{(i)}$  are the  $i$ th column of  $J_r$  and  $J_{s0}$ , respectively.

Using this analysis, we find that if  $J_{s0}$  is used to approximate the Jacobian throughout the workspace, the magnitude of the Jacobian will differ by as much as a factor of 0.7 and the direction by as much as 40°. Unsurprisingly,  $J_{s0}$  becomes a less accurate approximation at the edges of the workspace (further away from the straightforward configuration).

Performing the same analysis for the physical robot Jacobian, we find that it varies much more throughout the robot's workspace than the image space Jacobian. In particular, the physical robot Jacobian in the straightforward configuration differs by as much as a factor of 2 in magnitude and 110° in direction when used to approximate the physical robot Jacobian throughout its workspace. This discrepancy is large enough that an equivalent calibration routine would not work for task-space control of this robot. Instead a configuration-dependent, model-based Jacobian relying on known physical parameters that may change between uses of the robot would have to be used.

Another configuration consideration is robot length.  $\hat{J}_r$  is calibrated before growth and the length of the robot will continually increase during the growth process, which affects the image space Jacobian. As explained in the Growing Considerations section, the magnitude of  $J_r$  approximately scales with length. To account for this and inaccuracies in the calibrated Jacobian,  $\hat{J}_r$ , we choose controller gains  $K_p, K_d$  (Visual Servo Control Law section) that are more conservative than the optimal gains for steering of the robot just after Jacobian calibration. Concretely, if  $K_p^*$  and  $K_d^*$  are the optimal gains for steering just after calibration, we set  $K_p, K_d = K_p^*/2, K_d^*/2$ .

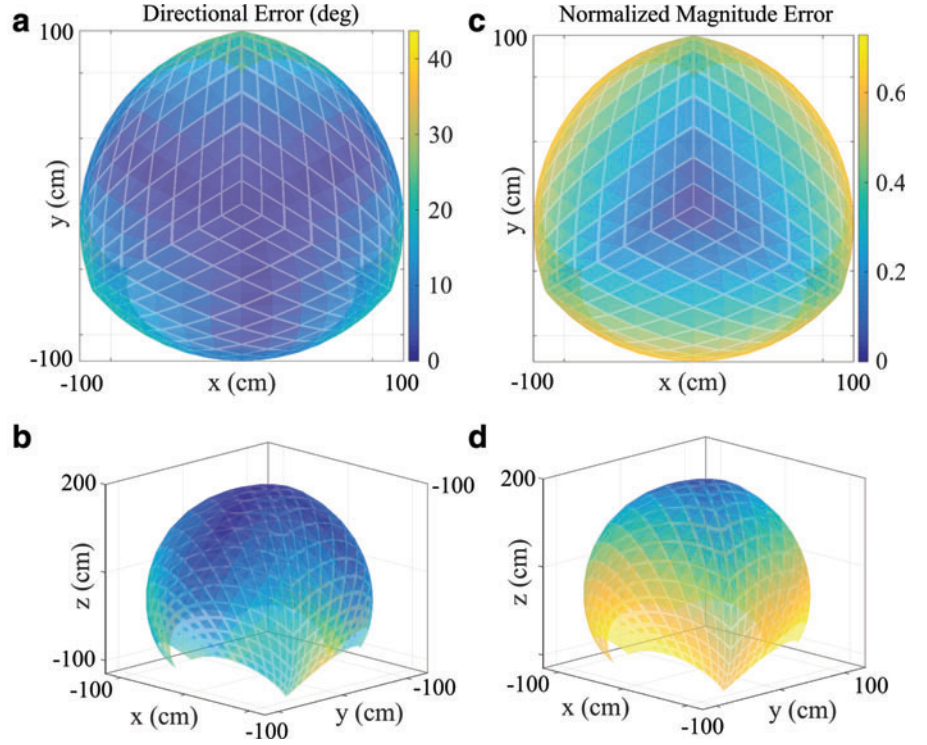
**Camera rotation.** As explained in the Image Space Modeling section, the camera is free to rotate about its optical axis as the robot grows (Fig. 10). Rotations about the optical axis are captured by the parameter  $\beta$ , which is the angle between the robot tip frame and camera reference frame.  $\beta$  is initially 0°. To account for camera rotation,  $\hat{J}_r$  must be continually updated to compensate for changes in  $\beta$ .

To estimate  $\beta$ , we use an IMU (Bosch BNO055) rigidly attached to the tip camera. The IMU provides an estimate of the direction of gravity,  $\hat{g} = [g_x, g_y, g_z]^\top$ , in the reference frame of the camera.  $\beta$  is computed from  $\hat{g}$  by computing the angle of its two-dimensional projection onto the plane of the camera:

$$\beta = \text{atan2}(g_y, g_x) - \text{atan2}(g_y^0, g_x^0) \quad (42)$$

where  $\hat{g}^0 = [g_x^0, g_y^0, g_z^0]^\top$  is the gravity vector when the tip frame and camera reference frame are aligned, that is,  $\beta = 0$ .

**FIG. 11.** Visualization of the consistency of the image Jacobian throughout the growing robot's workspace. **(a, b)** The directional consistency from the side and above, respectively. **(c, d)** The magnitude consistency from the side and above, respectively. Because the image Jacobian is slow to change throughout the robot's workspace, using a static Jacobian estimate in the visual servo control law (Visual Servo Control Law section) results in a stable controller. Color images available online at [www.liebertpub.com/soro](http://www.liebertpub.com/soro)



With an estimate of  $\beta$ ,  $\hat{J}_r$  is compensated to account for camera spin by a two-dimensional rotation:

$$\hat{J}_s^c = \begin{bmatrix} \cos(\beta) & \sin(\beta) \\ -\sin(\beta) & \cos(\beta) \end{bmatrix} \hat{J}_r \quad (43)$$

where  $\hat{J}_s^c$  is the compensated image Jacobian. This update equation is equivalent to updating  ${}^cV_f$  with the new value of  $\beta$  in Equation 25.

## Experimental Results

In this section, we present experiments that both characterize the growing robot and validate the kinematic models and control presented in this work.

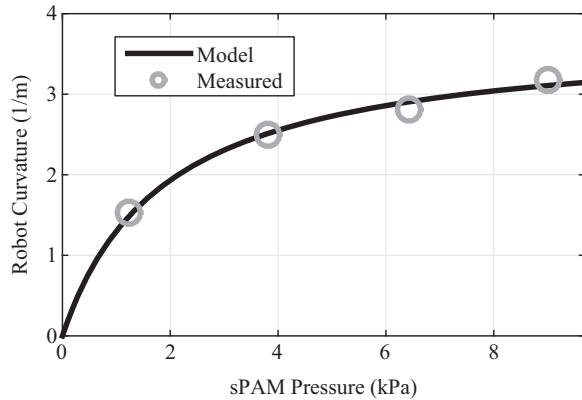


**FIG. 12.** The effect of a single sPAM actuator on robot bending. The curvature predicted by the kinematic model is shown in *black* and the measured curvature values are shown as *grey circles*. Curvature increases with sPAM pressure, but saturates as the sPAM reaches its maximum contraction ratio.

## Validation of kinematics of growth and steering

Rearrangement of the kinematic model equations (Eqs. 4–6) results in an equation that predicts the growing robot backbone curvature as a function of sPAM pressure:

$$\kappa = \frac{c_1 p}{c_2 p + 1} \quad (44)$$

where  $c_1, c_2$  are constants that depend on the physical parameters of the robot,  $p$  is the pressure in the sPAM, and  $\kappa$  is the backbone curvature of the growing robot.

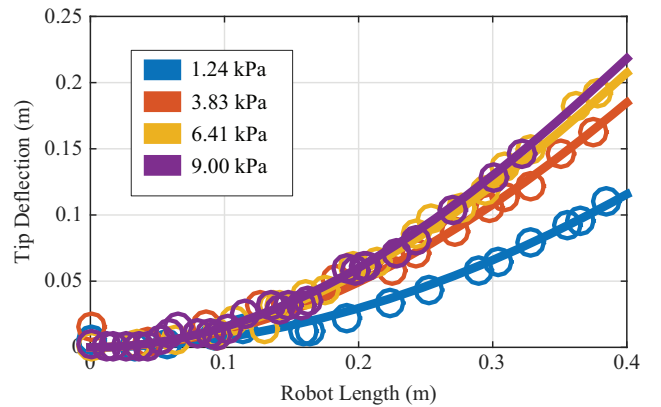


**FIG. 13.** Tip deflection from a straight-line trajectory versus length. Robot was grown four times with four different sPAM pressure values. Expected tip deflection for a robot grown with four sPAM pressures is plotted in *solid lines* and corresponding measurements are shown as *circles of the same color*. Model and measurements indicate robot grows with constant curvature with curvature predicted by plot in Figure 12. Color images available online at [www.liebertpub.com/soro](http://www.liebertpub.com/soro)

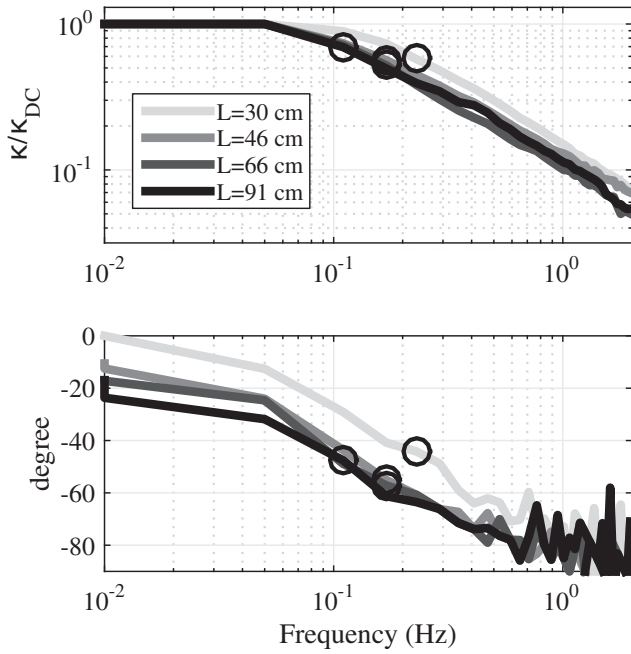


**FIG. 14.** Bode plot of open-loop robot bending (frequency versus backbone curvature amplitude) for several robot lengths. The robot exhibits first-order system behavior with a phase loss of  $\sim 90^\circ$  and cutoff frequency at  $\sim 45^\circ$  phase loss for all four tested robot lengths. Unsurprisingly, cutoff frequency drops with length indicating that the robot is capable of less responsive steering at larger lengths. Black circles mark the cutoff frequency of each Bode plot.

To derive Equation 44, as well as the values of  $c_1, c_2$ , we note in the case that a single sPAM is actuated (assume sPAM 1 without loss of generality),  $\phi = \psi_1$  and  $\phi_1 = 0$ . (Refer to Table 1 for variable definitions.) In this case, Equations 4–6 reduce to three scalar equations in three unknowns,  $l, l_1, \theta$ :

$$l_1 = l - \frac{D_{\text{tube}}}{2} \theta \quad (45)$$

$$0 = k_1 p_1 (l_1 - l_1^{\text{eq}}) - K(l - l^{\text{eq}}) \quad (46)$$

$$0 = \frac{D_{\text{tube}}}{2} k_1 p_1 (l_1 - l_1^{\text{eq}}) - K_l \theta \quad (47)$$

Solving this system of equations for  $l, l_1, \theta$  allows us to write down the robot's curvature  $\kappa = \frac{\theta}{l}$  as a function of actuator pressure,  $p_1$ , and physical robot parameters. Doing this, we find the following values for  $c_1$  and  $c_2$ , which depend only on fixed robot parameters:

$$c_1 = \frac{D_{\text{tube}} k_1 (l^{\text{eq}} - l_1^{\text{eq}})}{2 l^{\text{eq}} K_l} \quad (48)$$

$$c_2 = \frac{k_1 l_1^{\text{eq}} K_l + K k_1 l^{\text{eq}} D_{\text{tube}}}{K l^{\text{eq}} K_l} \quad (49)$$

We performed an experiment to verify the analysis of growth for the kinematic model presented in the Kinematics

of Growth and Steering section. In this experiment, the robot was grown four separate times with constant sPAM pressures of 0.18, 0.56, 0.93, and 1.31 pounds per square inch (PSI), respectively, in a single sPAM. These pressures were chosen to provide significant coverage of the curvature range. An overhead camera recorded the movement of the robot during the growth. Manual segmentation of the tip of the robot was performed roughly every 4 cm to yield a time-series of tip positions of the robot as it was grown. At the end of each trial, a curvature value was fit to the backbone of the grown robot using manual segmentation and the results are shown as gray circles in Figure 12.

The curvature parameters,  $c_1, c_2$ , were chosen to minimize the difference between the curvature values predicted in Equation 44 and measured curvature values. The resulting curve is shown in Figure 12. The robot starts straight (zero curvature) when there is no pressure in the sPAMs. Curvature increases rapidly at low-pressure values, but saturates due to the finite strain that is achievable by an sPAM.

Based on the fit curvature values, we predicted the expected tip deflection from a straight-line trajectory over the course of the four growth trials. According to the Kinematics

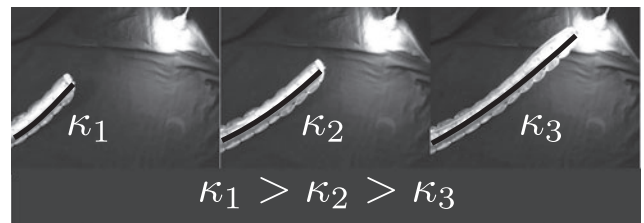
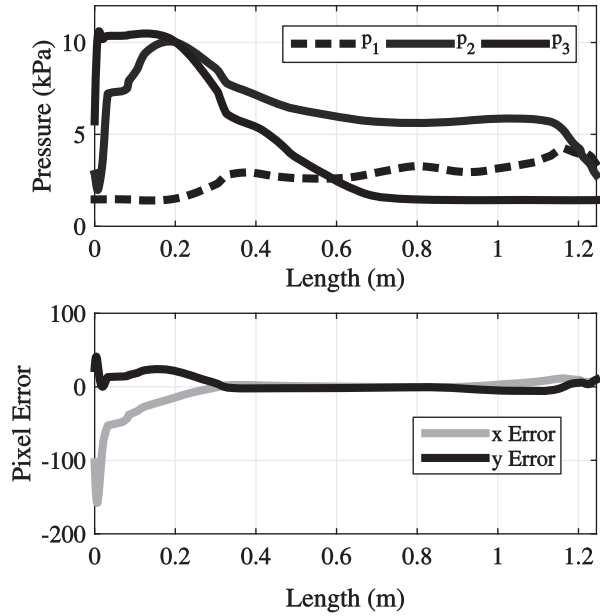


**FIG. 15.** Growing and steering to a light. To maintain heading alignment with the light as the robot's length increases, the steering controller must continually decrease the curvature of the robot by decreasing the pressure in the sPAMs. This behavior is not explicitly programmed in the visual servo control law, but happens as an indirect consequence of keeping the light at the center of its tip camera image (indicated by zero pixel error). Still-frame images are shown at three times during its growth with corresponding decreasing curvatures  $\kappa_1, \kappa_2, \kappa_3$ .

of Growth and Steering section, we expect the robot to grow with constant curvature since the pressure in the sPAMs was held constant. Figure 13 shows the predicted tip deflection values along with measured tip deflection values as a function of backbone length. As can be seen, there is strong agreement between predicted and measured tip deflection, indicating that the robot does grow with constant curvature. In addition, this experiment supports the analysis in the Growing Considerations section, which means that steering controller gains must be selected more conservatively when the controller is tuned with a robot that is at a shorter length.

#### sPAM dynamic response

We performed an experiment to measure the dynamic response of open-loop bending of the growing robot held at a constant length. To understand how length affected the bending behavior of the robot, we generated experimental Bode plots of bending curvature versus frequency of growing robots of four different lengths: 30, 46, 66, and 91 inches. A red- and blue-colored fiducial was attached to the tip of the robot several centimeters apart along its backbone to facilitate automated measurement of tip orientation using an overhead camera. A sinusoidal sweep of pressures in a frequency range of 0 to 2 Hz was commanded to create a sinusoidally varying backbone curvature. Two sPAMs placed radially opposite one another were used in the experiment to enable bending in opposite directions ( $\phi = 0^\circ, 180^\circ$ ).

Curvature amplitude was measured from tip orientation at a particular frequency,  $\omega$ , by setting  $\kappa_\omega = (\theta_{\max} - \theta_{\min})/2$  where  $\theta_{\max}, \theta_{\min}$  were the maximum and minimum tip orientations measured in the  $\omega$  frequency portion of the sinusoidal sweep. Phase information was extracted using a light emitting diode that was activated at the beginning of a new frequency so that precise synchronization between the video and commanded pressures could be determined. Figure 14

shows the experimental Bode plot of normalized curvature versus frequency for each of the four lengths.

All four robot lengths had a cutoff frequency (frequency at which curvature magnitude ratio drops below  $1/\sqrt{2}$ ) of less than 0.5 Hz (indicated by the black circles in Fig. 14), with cutoff frequency monotonically decreasing with increasing robot length. Dynamic response is most likely limited by flow rate of the regulators used to inflate the sPAMs. Although the robot has low bandwidth in the large curvature changes that are needed for volitional direction changes of the robot, its bandwidth is higher for smaller amplitude curvature changes, which are needed to maintain heading alignment during robot growth.

#### Growing to a goal location

Several experiments were performed to demonstrate the robot's ability to grow and steer to a designated object using the visual servo control law described in the Visual Servo Control Law section.

Figure 15 shows a sequence of still-frame images of the robot growing to a light as well as the pressures that were commanded by the visual servo steering controller. The corresponding pressure plot shows the robot starting with high pressure in two of its three sPAMs. These sPAM pressures cause the robot to bend so that its heading is aligned with the light. As the robot lengthens, the steering controller decreases pressure in its sPAMs to maintain a straight-line trajectory that is aligned with the light. If it did not lower pressure, the robot would oversteer, as seen in Figure 13. The visual servo controller is able to accomplish this behavior by maintaining the light at the center of its tip camera image without explicit consideration of growth or curvature.

More complicated growth trajectories are shown in Figures 16 and 17. Both figures feature the robot's ability to navigate paths that are not constant curvature. In Figure 16, the robot is first steered into a tunnel by designating the

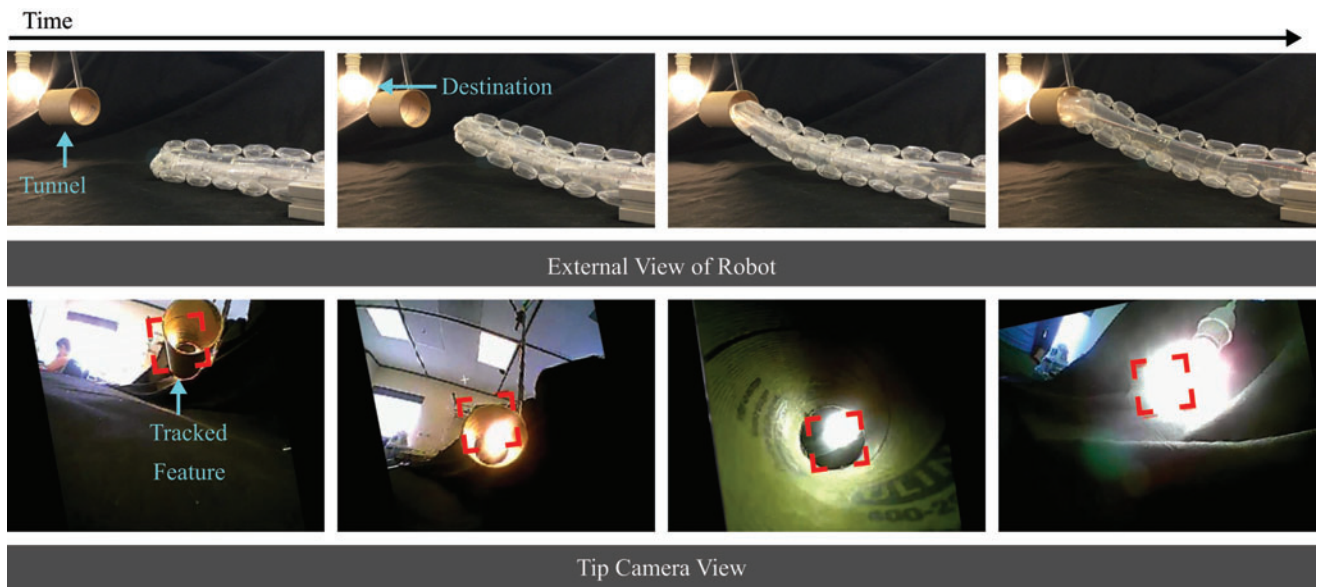


**FIG. 16.** Two image sequences showing the robot growing to a light via a tunnel. *Top row* is an image sequence of the robot and *bottom row* is an image sequence from the robot's tip camera. Each image pair in a *column* is time aligned. Time progresses to the right, and the first image is from the moment after the steering controller was turned on. The right-most image is an overhead view of the robot. The *light* is the designated point the robot is moving toward in the figure. Color images available online at [www.liebertpub.com/soro](http://www.liebertpub.com/soro)



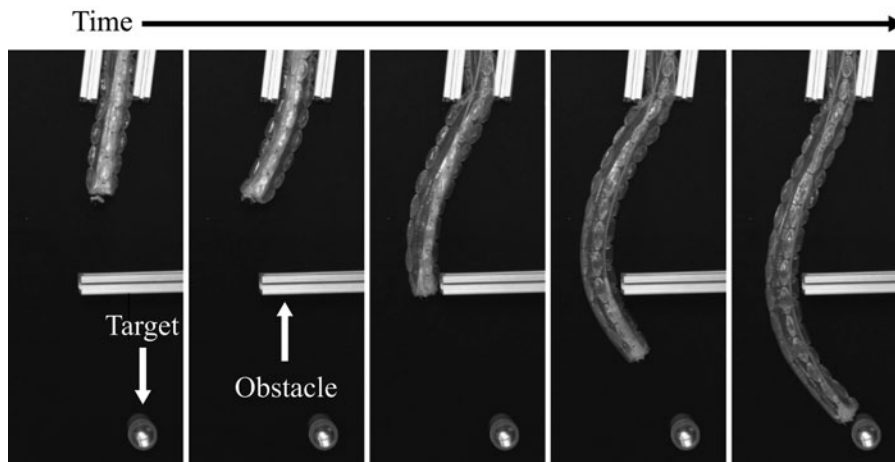


**FIG. 17.** Growth around an obstacle. First the robot is steered to a waypoint to the left of the obstacle and then to the destination.

tunnel's entrance as the tracked feature for the visual servo controller. Once inside the tunnel, the controller's destination was changed to the light. Although the robot's body is constrained by the tunnel, it is able to grow to a new destination after leaving the tunnel without modification to the control law. In Figure 17, the robot must first make it around an obstacle before reaching its destination. To accomplish this, the robot was first steered to a waypoint to the left of the obstacle before being steered to its destination. In both cases, the visual servo controller is successful even though the robot takes on nonconstant curvature shapes.

### Conclusions and Future Work

This article presents the design, modeling, and control of a new soft continuum robot that has a tip extension degree of freedom. The tip extension degree of freedom creates movement in the direction of the robot's tip tangent. Among other benefits, this simplifies the control of the robot through decoupled steering and forward movement. Extension of the robot is realized using pneumatically driven tip eversion.

In contrast to the robot presented in Hawkes *et al.*,<sup>18</sup> which turns at small, discrete intervals along its length by permanently changing its shape, the robot introduced in this article steers using reversible bending of the robot's backbone to deflect the robot from a straight path. There are several trade-offs between the two methods of steering that may make one mechanism more advantageous for a given use case. Reversible bending gives the operator the ability to look around the robot's environment by reorienting the robot's tip. In addition, corrections to the robot's heading can be made as the robot is growing, which is particularly advantageous for scenarios where accurate alignment is needed, such as growing into a tunnel (Fig. 16).

However, the robot from Hawkes *et al.*<sup>18</sup> has an advantage in very delicate environments, because the body's shape does not change during steering. In contrast, for the robot presented here, the entire length of the body may move during steering, resulting in environmental contact. The robot in Hawkes *et al.*<sup>18</sup> moves according to follow-the-leader motion, which has the advantage that its body does not move once it is grown, but has the disadvantage that the robot must grow to turn. Because steering decisions are made at discrete intervals and are permanent, stability of the steering controller is not a concern for the irreversible turning mechanism

of Hawkes *et al.*<sup>18</sup> This is not the case for the robot in this work, where steering gains must be selected with care (Visual Servo Control Law section). Ultimately, the optimal turning solution for growing robots may be a combination of the turning mechanisms presented in this article and Hawkes *et al.*<sup>18</sup> Future work will investigate new actuator design and control that combine features of both steering methods. In addition, we would like to demonstrate reversible steering at the length scales of tens of meters, as described in Hawkes *et al.*,<sup>18</sup> and also at diameter scales of millimeters.

### Acknowledgments

This work was supported, in part, by the National Science Foundation grant 1441358 and Air Force Office of Scientific Research grant FA2386-17-1-4658.

### Author Disclosure Statement

No competing financial interests exist.

### References

1. Burgner-Kahrs J, Rucker DC, Choset H. Continuum robots for medical applications: a survey. *IEEE Trans Robot* 2015; 31:1261–1280.
2. Dupont PE, Lock J, Itkowitz B, *et al.* Design and control of concentric-tube robots. *IEEE Trans Robot* 2010;26:209–225.
3. Webster III RJ, Romano JM, Cowan NJ. Mechanics of precurved-tube continuum robots. *IEEE Trans Robot* 2009; 25:67–78.
4. Neppalli S, Jones B, McMahan W, *et al.* Octarm-a soft robotic manipulator. In: *IEEE/RSJ International Conference on Intelligent Robots and Systems*, San Diego, CA: IEEE, 2007, pp. 2569–2569.
5. Mehling JS, Diftler MA, Chu M, *et al.* A minimally invasive tendril robot for in-space inspection. In: *IEEE/RAS-EMBS International Conference on Biomedical Robotics and Biomechatronics*, Pisa, Italy: IEEE, 2006, pp. 690–695.
6. Walker ID. Continuous backbone “continuum” robot manipulators. *ISRN Robotics* 2013;2013:726506.
7. Gravagne IA, Rahn CD, Walker ID. Large deflection dynamics and control for planar continuum robots. *IEEE ASME Trans Mechatron* 2003;8:299–307.

8. Webster RJ, Jones BA. Design and kinematic modeling of constant curvature continuum robots: a review. *Int J Rob Res* 2010;29:1661–1683.
9. Yip MC, Camarillo DB. Model-less feedback control of continuum manipulators in constrained environments. *IEEE Trans Robot* 2014;30:880–889.
10. McMahan W, Jones BA, Walker ID. Design and implementation of a multi-section continuum robot: Air-octor. In: *IEEE/RSJ International Conference on Intelligent Robots and Systems (IROS)*, San Diego, CA: IEEE, 2005, pp. 2578–2585.
11. Immega G, Antonelli K. The KSI tentacle manipulator. In: *IEEE International Conference on Robotics and Automation (ICRA)*, Nagoya, Japan: IEEE, 1995, Vol. 3, pp. 3149–3154.
12. Mishima D, Aoki T, Hirose S. Development of pneumatically controlled expandable arm for search in the environment with tight access. In: *Field and Service Robotics*. Berlin, Germany: Springer, 2003, pp. 509–518.
13. Rösch T, Adler A, Pohl H, *et al.* A motor-driven single-use colonoscope controlled with a hand-held device: a feasibility study in volunteers. *Gastrointest Endosc* 2008;67: 1139–1146.
14. Sadeghi A, Tonazzini A, Popova L, *et al.* Robotic mechanism for soil penetration inspired by plant root. In: *2013 IEEE International Conference on Robotics and Automation (ICRA)*, Karlsruhe, Germany: IEEE, 2013, pp. 3457–3462.
15. Del Dottore E, Mondini A, Sadeghi A, *et al.* Circumnutations as a penetration strategy in a plant-root-inspired robot. In: *IEEE International Conference on Robotics and Automation (ICRA)*, Stockholm, Sweden: IEEE, 2016, pp. 4722–4728.
16. Sadeghi A, Tonazzini A, Popova L, *et al.* A novel growing device inspired by plant root soil penetration behaviors. *PLoS One* 2014;9:2.
17. Tsukagoshi H, Arai N, Kiryu I, *et al.* Tip growing actuator with the hose-like structure aiming for inspection on narrow terrain. *Int J Autom Technol* 2011;5:516–522.
18. Hawkes EW, Blumenschein LH, Greer JD, *et al.* A soft robot that navigates its environment through growth. *Sci Robot* 2017;2:eaan3028.
19. Greer JD, Morimoto TK, Okamura AM, *et al.* Series pneumatic artificial muscles (sPAMs) and application to a soft continuum robot. In: *IEEE International Conference on Robotics and Automation (ICRA)*, Singapore: IEEE, 2017, pp. 5503–5510.
20. Camarillo DB, Milne CF, Carlson CR, *et al.* Mechanics modeling of tendon-driven continuum manipulators. *IEEE Trans Robot* 2008;24:1262–1273.
21. Chou C-P, Hannaford B. Measurement and modeling of mckibben pneumatic artificial muscles. *IEEE Trans Rob Autom* 1996;12:90–102.
22. Klute GK, Czerniecki JM, Hannaford B. Mckibben artificial muscles: pneumatic actuators with biomechanical intelligence. In: *IEEE/ASME International Conference on Advanced Intelligent Mechatronics*, Atlanta, GA: IEEE, 1999, pp. 221–226.
23. Niiyama R, Sun X, Sung C, *et al.* Pouch motors: printable soft actuators integrated with computational design. *Soft Robot* 2015;2:59–70.
24. Daerden F. Conception and Realization of Pleated Pneumatic Artificial Muscles and Their Use as Compliant Actuation Elements. Belgium: Vrije Universiteit Brussel, 1999.
25. Hawkes EW, Christensen DL, Okamura AM. Design and implementation of a 300% strain soft artificial muscle. In: *IEEE International Conference on Robotics and Automation*, Stockholm, Sweden: IEEE, 2016, pp. 4022–4029.
26. Usevitch NS, Okamura AM, Hawkes EW. Antagonistic pneumatic artificial muscle. In: *IEEE International Conference on Robotics and Automation*, Brisbane, QLD, Australia: IEEE, 2018, pp. 1539–1546.
27. Flandin G, Chaumette F, Marchand E. Eye-in-hand/eye-to-hand cooperation for visual servoing. In: *IEEE International Conference on Robotics and Automation*, San Francisco, CA: IEEE, 2000, Vol. 3, pp. 741–746.
28. Daerden F, Lefeber D. The concept and design of pleated pneumatic artificial muscles. *Int J Fluid Power* 2001;2:41–50.
29. Howell LL. *Compliant Mechanisms*, Hoboken, NJ: John Wiley & Sons, 2001.
30. Ikeuchi K. *Computer Vision: A Reference Guide*, New York, NY: Springer Publishing Company, Inc., 2014.
31. Espiau B, Chaumette F, Rives P. A new approach to visual servoing in robotics. *IEEE Trans Rob Autom* 1992;8:313–326.
32. Chaumette F, Hutchinson S. Visual servo control. i. basic approaches. *IEEE Robot Autom Mag* 2006;13:82–90.
33. Stark PB, Parker RL. Bounded-variable least-squares: an algorithm and applications. *Comput Stat* 1995;10:129–129.

Address correspondence to:

*Joseph D. Greer*

*Department of Mechanical Engineering*

*Stanford University*

*Stanford, CA 94305*

*E-mail: jdgreer@stanford.edu*